

1 For submission to Atmospheric Chemistry and Physics

2

3 Degree of ice particle surface roughness in-
4 ferred from polarimetric observations

5 S. Hioki¹, P. Yang¹, B. A. Baum², S. Platnick³, K. G. Meyer⁴, M. D. King⁵, J.
6 Riedi⁶

7 [1]{Department of Atmospheric Sciences, Texas A&M University, College Station,
8 Texas}

9 [2]{Space Science and Engineering Center, University of Wisconsin-Madison, Madi-
10 son, Wisconsin}

11 [3]{Earth Science Division, NASA Goddard Space Flight Center, Greenbelt, Maryland}

12 [4]{Goddard Earth Sciences Technology and Research, Universities Space Research
13 Association, Columbia, Maryland}

14 [5]{Laboratory for Atmospheric & Space Physics, University of Colorado, Boulder,
15 CO}

16 [6]{Laboratoire d'Optique Atmosphérique, Université de Lille - Sciences et Technol-
17 ogies, Villeneuve d'Ascq, France}

18

19

20 Correspondence to S. Hioki (s.hioki@tamu.edu)

21 **Abstract**

22 The degree of surface roughness of ice particles within thick, cold ice clouds is in-
23 ferred from multi-directional, multi-spectral satellite polarimetric observations over
24 oceans, assuming a column-aggregate particle habit. An improved roughness infer-
25 ence scheme is employed that provides a more noise-resilient roughness estimate
26 than the conventional best-fit approach. The improvements include the introduction

1 of a quantitative roughness parameter based on empirical orthogonal function anal-
2 ysis and proper treatment of polarization due to atmospheric scattering above
3 clouds. A global one-month data sample supports the use of a severely roughened
4 ice habit to simulate the polarized reflectivity associated with ice clouds over ocean.
5 The density distribution of the roughness parameter inferred from the global one-
6 month data sample and further analyses of a few case studies demonstrate the sig-
7 nificant variability of ice cloud single-scattering properties. However, the present
8 theoretical results do not agree with observations in the tropics. In the extratropics,
9 the roughness parameter is inferred but 74% of the sample is out of the expected
10 parameter range. Potential improvements are discussed to enhance the depiction of
11 the natural variability on a global scale.

12

13 **1. Introduction**

14 Satellite observations at visible and infrared wavelengths can characterize
15 global cloud microphysical parameters and radiative properties. Numerous
16 techniques have been developed to retrieve ice cloud optical and microphysical
17 properties from radiometric measurements (e.g., Inoue, 1987; Nakajima and King,
18 1990; Minnis et al., 1993) and have been adopted in operational retrieval efforts
19 (Rolland et al., 2000; Platnick et al., 2003; Minnis et al., 2011). A synergetic
20 combination of satellite and in-situ observations (e.g., Heymsfield et al., 2002, 2013)
21 serves as a constraint for the parameterization of bulk ice cloud optical properties
22 for remote sensing implementations as well as general circulation models (GCMs).

23 The accuracy of these retrieval techniques and the validity of downstream
24 applications including GCM radiation parameterization hinges on steady
25 improvements in the single-scattering calculations involving ice crystals. As ice
26 clouds consist of nonspherical particles with characteristic sizes much larger than

1 the wavelengths of interest, the single-scattering properties depend on the size,
2 shape, and microscopic morphology of the particles (Macke et al., 1996; Yang et al.,
3 2008a; Xie et al., 2009; Baum et al., 2010; Um and McFarquhar 2007, 2009;
4 Ulanowski et al., 2006, 2014). In the solar shortwave spectrum, particle shape,
5 surface texture, and crystal imperfections have a substantial influence on the single-
6 scattering properties. Recent improvements in scattering calculation techniques are
7 being incorporated into models that represent diverse ice particle populations in
8 clouds.

9 However, it is challenging to quantify some of these influential microphysical
10 parameters, given current satellite sensors. As a result, little information about their
11 variability is available. The discrepancies among climate models (Waliser et al.,
12 2009) in terms of ice water path (IWP) indicate that the GCM parameterizations
13 need more reliable constraints on IWP. Recent work by Sourdeval et al. (2015),
14 which includes direct retrieval of IWP, is a novel approach to this problem.

15 The ability of passive and lidar sensors to correctly infer IWP requires
16 knowledge of ice cloud radiative properties. Application of an unrealistic ice model,
17 e.g., with only smooth (unroughened) surfaces, results in an overall global bias
18 (Macke and Mishchenko 1996; Yang et al., 2007, 2008b; Holz et al. 2015) as well as
19 seasonal biases (Zhang et al., 2009) in cloud property retrievals. The overarching
20 goal of this paper is to gain a better understanding of the constraints in the
21 microphysical parameters of global ice clouds using angular polarimetric
22 observations and state-of-the-art light-scattering computational capabilities.

23 Multidirectional polarimetric observations can constrain the representative
24 particle shape and surface texture condition (specifically, the degree of surface
25 roughness), owing to the sensitivity of the polarization state of reflected light to
26 small-scale particle structures. These measurements have been used to infer both
27 particle habit (Chepfer, 1998; C.-Labonnote et al., 2001; Masuda et al., 2002; Knap et

1 al., 2005; Baran and C.-Labonnote, 2007) and surface roughness (Baran and C.-
2 Labonnote, 2006; Cole et al., 2013, 2014). Since polarized reflectivity saturates at
3 relatively small optical thickness (generally about $\tau = 5$, Masuda and Takashima,
4 1992), the conventional “best-fit” approach to this problem computes the residual
5 sum of squares (RSS) from the multi-angle observations of polarized reflectivity and
6 reflectivity simulations, and selects the ice particle model that minimizes the RSS
7 when $\tau > 5$.

8 The previous studies imply that the use of roughened particles is necessary to
9 achieve maximum consistency between observations and numerical scattering
10 calculations. Furthermore, the spectral consistency of visible/near-infrared and
11 thermal infrared retrievals (Baran and Francis 2004) was recently investigated by
12 Liu et al. (2015) and Holz et al. (2015), who report that retrieved ice cloud optical
13 thicknesses are more consistent when a particle is roughened.

14 The treatment of particle surface roughness here is not a rigorous approach.
15 Rather, it is an approximation of the effects of roughened surface texture (Neshyba
16 et al., 2013) and other kinds of imperfections present in natural ice cloud particles.
17 The scattering property calculated by this approximate method is in reasonable
18 agreement with that calculated by rigorous ray-tracing methods (Yang et al., 2008a).
19 Although previous studies suggest that some degree of roughness is desirable, the
20 issue remains as to the amount of roughness that should be adopted for global
21 satellite-based retrievals, or used in numerical models.

22 Recent work by van Diedenhoven et al. (2012, 2014) simultaneously infers both
23 the aspect ratio and the degree of roughness from a combination of polarimetric and
24 intensity observations over a virtually continuous parameter space, assuming that
25 simple hexagonal ice particles can explain observations. The ability to infer a
26 representative ice cloud particle aspect ratio adds yet another dimension to the
27 problem. Such exploration into the variability of ice particle microphysical

1 properties can lead to a more reliable satellite climatology of ice clouds. This study
2 focuses on the quantitative inference of ice particle roughness parameter for a
3 specific particle habit, and will not include a detailed investigation of aspect ratio.

4 While a conventional “best-fit” approach can constrain the range of the average
5 roughness parameter at the global scale, it is not suitable for the pixel-by-pixel
6 inferences. This is because the signal-to-noise ratio for particle roughness is low,
7 and in the conventional “best-fit” approach, even random observational errors can
8 modify the inferred histogram significantly when it is applied to individual pixels.
9 Figure 1 illustrates how such a modification takes place if the method is applied to a
10 synthetic signal with random noise. To produce Fig. 1, viewing geometries are
11 extracted from one month (September 2005) of cloud observations by the
12 POLarization and Directionality of the Earth’s Reflectance (POLDER) sensor
13 (Deschamps et al., 1994) onboard the Polarization and Anisotropy of Reflectances
14 for Atmospheric Sciences coupled with Observation from Lidar (PARASOL) satellite
15 (Fougnie et al., 2007). The “best-fit” inference is applied to synthetic multi-angle
16 cloud polarized reflectivities (L_p , defined in Section 2.1) with and without random
17 noise. In synthesizing the signal, a column aggregate particle shape (e.g. Yang et al.,
18 2013) is assumed with a roughness parameter of $\sigma^2 = 0.15$ (variance of the slope of
19 random facet tilts, see Yang et al., 2008b for details), and the random error has a
20 normal distribution with variance equivalent to the POLDER observational error,
21 which is estimated in Section 2.1. The hatched bar is the histogram with noise and
22 the gray bar is that without noise. Note that the distinct peak at $\sigma^2 = 0.15$ is no
23 longer apparent when instrumental noise is included, indicating the necessity of
24 appropriate treatment of the error distribution in the analysis.

25 This paper demonstrates how a continuous parameter space for the roughness
26 retrieval is constructed and how it can be used to infer the particle roughness of
27 optically thick ice clouds on a pixel-by-pixel basis. Section 2 provides the details of

1 the data and inversion method we employed, and the result of the application to one
2 month of global data is described in Section 3. Concluding remarks are given in
3 Section 4.

4

5 **2 Methodologies**

6 To establish a method resilient to observational error, we first scrutinize
7 random errors in POLDER data and select pixels based on the MODIS Collection 6
8 cloud product, as given in Section 2.1. Then, a continuous parameter space for
9 inferring roughness is constructed by using an empirical orthogonal function
10 analysis, and used in the retrieval scheme with the maximum likelihood method.
11 The construction of the parameter space, and the design and the performance of the
12 forward model, are discussed in Section 2.2.

13

14 **2.1 Observations**

15 **2.1.1 Reflectivity from POLDER**

16 The POLDER sensor onboard the PARASOL satellite provides multispectral
17 polarimetric observations at up to 16 viewing geometries for a single overpass
18 (Fougnie et al., 2007). The PARASOL satellite was in the A-train satellite
19 constellation from 2004 to 2009 and continued operation in a separate orbit until
20 late 2013, providing a total of nine years of global polarimetric observation data.
21 The design of the instrument is inherited from previous POLDER sensors on the
22 ADEOS (ADvanced Earth Observing Satellite) platforms. POLDER sensors provide
23 the first three elements of the Stokes vector from three images taken successively
24 with linear polarization filters (Deschamps et al., 1994).

1 This study uses the single-pixel data set in PARASOL Level 1B product (i.e. the
2 approximate resolution is $6 \text{ km} \times 6 \text{ km}$).

3 PARASOL products report the intensity of reflection in terms of normalized
4 radiance L_n , which is equal to the reflectivity R of the surface-atmosphere system
5 multiplied by the factor $\mu_0 = \cos \theta_0$ (cosine of solar zenith angle).

$$L_n(\mu, \mu_0, \varphi, \varphi_0) = \mu_0 R(\mu, \mu_0, \varphi, \varphi_0) \quad (1)$$

6 The reflectivity R is defined as

$$R(\mu, \mu_0, \varphi, \varphi_0) = \frac{\pi I(\mu, \mu_0, \varphi, \varphi_0)}{E_0 \mu_0} \quad (2)$$

7 where $I(\mu, \mu_0, \varphi, \varphi_0)$ is the radiance and $E_0 \mu_0$ is the irradiance of incoming unpolar-
8 ized light (i.e., solar irradiance; E_0 is the beam flux).

9 In a similar manner, the polarized reflectivity is reported in terms of normalized
10 radiance, so (L_n, Q, U) become the first three Stokes parameters. In other words, the
11 normalized polarized radiance $L_{np} = \sqrt{Q^2 + U^2}$ is equal to the polarized reflectivity
12 R_p multiplied by μ_0 .

$$L_{np}(\mu, \mu_0, \varphi, \varphi_0) = \mu_0 R_p(\mu, \mu_0, \varphi, \varphi_0) = \frac{\pi \sqrt{Q_i^2 + U_i^2}}{E_0 \mu_0}, \quad (3)$$

13 where Q_i and U_i are defined to form the first three Stokes parameters in terms of
14 radiance (I, Q_i, U_i) . It is worth noting the similarity between Eqs. (1) and (3). We
15 conduct the analysis in terms of $L_{np} = \mu_0 R_p$ defined in Eq. (3) to simplify the error
16 estimate.

17 The distribution of random errors in L_{np} observed with POLDER is estimated in
18 the following procedure. A reflection property of an optically thick ice cloud is that
19 the modified polarized reflectivity $L_{nmp} = \eta(\mu + \mu_0)L_p/\mu_0$ (where $\eta = \pm 1$, C.-
20 Labonnote et al., 2001) crosses zero at scattering angle $\Theta \approx 170^\circ$ as shown in Fig. 2.

1 This implies that the polarization signal at $\Theta \approx 170^\circ$ is primarily due to the
 2 observational noise with additional contributions from the variation of cloud
 3 particle scattering properties. We utilize this reflection property to estimate the
 4 magnitude of observational noise from the POLDER data at scattering angles
 5 between 168° and 172° , and further estimate the noise level at other angles with a
 6 typical polarization state of cloud reflection.

7 The POLDER observational noise consists of radiometric noise and misregistra-
 8 tion noise. The misregistration noise is inherent in the POLDER sensor's design that
 9 extracts polarimetric information from three images successively taken with
 10 different polarizers. The co-registration process of these three images is an
 11 inevitable source of error. As the distribution of misregistration noise is unknown,
 12 our instrument model attempts to explain both noise components with a
 13 radiometric noise model in the following analysis.

14 We define a random variable L_{np} that serves as a statistical model of observed
 15 L_{np} as follows.

$$L_{np} = \sqrt{X_1^2 + X_2^2 + X_3^2 - X_1X_2 - X_2X_3 - X_3X_1} \quad (4)$$

16 where random variables X_1 , X_2 , and X_3 represent the radiances of a pixel in the orig-
 17 inal three images with different polarizers (not available in a product). With the sta-
 18 tistical model outlined in Eq. (4), we first assume that X_1 , X_2 , and X_3 follow the same
 19 normal distribution centered at 0.5 with variance s^2 (i.e., $X_i \sim N(0.5, s^2)$) because the
 20 expectation of polarized radiance L_{np} is assumed to be zero at scattering angles be-
 21 tween 168° and 172° . With this assumption, we apply the parametric bootstrap
 22 method (e.g., Evans and Rosenthal, 2010) to obtain the distribution of L_{np} as a func-
 23 tion of variance s^2 . The observational distribution of L_{np} at $0.865 \mu\text{m}$ channel in the
 24 scattering angles between 168° and 172° (within the rectangular box in Fig. 2) is

1 shown in the bar chart of Fig. 3, and compared with the theoretical distribution with
2 $s = 0.00095$ (solid line). Figure 4 justifies our selection of $s = 0.00095$ by showing
3 that the sum of squared errors of the density in each bin of the histogram (Fig. 3) is
4 minimized when $s = 0.00095$. Therefore, we take $s = 0.00095$ as the standard er-
5 ror for X_1, X_2 , and X_3 . In Fig. 3, the distribution from observations is slightly more
6 skewed than the distribution from bootstrapping, but their agreement justifies the
7 use of the simple statistical model formulated in Eq. (4) to quantify the magnitude of
8 measurement errors.

9 To obtain the approximate magnitude of the L_{np} error at other scattering
10 angles, the same parametric bootstrap method is applied with the degree of linear
11 polarization fixed at 5%, which is the upper limit for typical ice cloud reflection. This
12 selection does not significantly affect the following analysis. When the signal is
13 polarized, random variables X_1, X_2 , and X_3 do not follow the same distribution, but
14 we assume that the standard errors for X_1, X_2 , and X_3 still stay the same. Figure 5
15 shows the estimated magnitude of error (variance) as a function of normalized
16 radiance L_n . The variance of L_{np} asymptotes to a near-constant value once L_n
17 reaches $L_n = 0.2$. As shown in insets, the distribution becomes closer to a normal
18 distribution with increasing L_n . Based on the discussion above, we conclude that the
19 error distribution of L_{np} approximately follows a normal distribution with variance
20 $\text{var}(L_{np}) = 1.35 \times 10^{-6}$ for a reflective target ($L_n \geq 0.2$). This estimate of error is
21 about the same magnitude as the value by Fougnie et al. (2007). Note that we
22 assume that the error is purely from observational noise, neglecting any natural
23 cloud variability. Therefore, the actual radiometric noise level should be somewhat
24 smaller than our estimate. We estimate the magnitude of error using the $0.856 \mu\text{m}$
25 channel because the channel is likely to be the least contaminated by other sources
26 of uncertainty such as ozone absorption ($0.67 \mu\text{m}$) and Rayleigh scattering ($0.49 \mu\text{m}$,

1 0.67 μm). We apply the same variance to all three POLDER channels used in the
2 analysis (0.865, 0.67, and 0.49 μm).

3 **2.1.2 Ancillary Data from MODIS and AIRS**

4 The MODerate resolution Imaging Spectroradiometer (MODIS) instruments
5 onboard the Aqua and Terra satellites measure radiance at multiple visible and
6 infrared wavelengths, providing various products (King et al., 2003) that are
7 complementary to those from PARASOL. Of interest here is the Collection 6 Level 2
8 cloud product (MYD06) from Aqua MODIS, with which the PARASOL satellite was
9 flying in formation until 2009. Cloud top temperature and thermodynamic phase are
10 extracted from MYD06 and are collocated to POLDER data to be used in the analysis
11 described later in this section. In addition, Level 3 monthly mean ozone
12 concentration from the Atmospheric Infrared Sounder (AIRS) on the Aqua satellite
13 is also used, in particular to account for absorption by ozone that attenuates
14 reflected radiation in the visible range.

15 **2.1.3 Collocation and Selection**

16 The PARASOL Level 1 radiometric data is first collocated with the MODIS Level
17 2 cloud product (Platnick et al., 2015) to select pixels containing ice clouds. Only
18 PARASOL pixels that have corresponding MODIS observations are selected, and
19 filtered by the criteria summarized in Table 1. The intent of the filtering process is to
20 avoid cloud edge contamination, to avoid supercooled water droplets, and to select
21 pixels where clouds are optically thick. The selection criterion of 208 K is a
22 threshold used to identify convective precipitation in the tropics (Mapes and Houze,
23 1993). The analysis is applied only over oceans so the influence of surface reflection
24 is minimal.

25 A “pixel” in the PARASOL Level 1 product contains multiple reflectivity data
26 observed from up to 16 viewing geometries. Individual reflectivity data stored in a

1 pixel is called a “view”, and we select valid views using criteria relating to scattering
2 angle and sunglint angle (see Table 1). When five or more valid views are contained
3 in a pixel that satisfy all pixel criteria previously mentioned, the pixel is marked as
4 valid, and the roughness inference is attempted.

5 **2.2 Inversion Methods**

6 **2.2.1 Selection of Retrieval Parameters**

7 To overcome the problem of the conventional “best-fit” approach that uses a
8 discrete set of roughness parameters, we construct a continuous parameter space
9 for the particle roughness with empirical orthogonal functions (EOF). The goal of
10 the EOF analysis is to find the parameter space that describes the variation of the
11 $-P_{12}$ element of the phase matrix when varying the particle roughness. An ideal
12 approach would be to use a collection of $-P_{12}$ values from observations (Rodgers,
13 2000), but such a dataset is unavailable. For this reason, we apply EOF analysis to
14 the $-P_{12}$ simulated with light scattering calculations. The first and second EOFs
15 together explain 99.3% of the entire variation of $-P_{12}$ in the scattering angle range
16 from 60° to 160° , so $-P_{12}$ for a particle of any roughness can be reconstructed
17 almost exactly from the first and second EOFs by a simple linear combination. Also,
18 $-P_{12}$ for a mixture of particles with different roughness parameters can be
19 reconstructed by the same linear combination.

20 The details of the particle model are as follows. The EOF analysis is applied to
21 $-P_{12}$ elements of the phase matrices calculated by the method described by Yang et
22 al. (2013), which is a combination of the Improved Geometric Optics Method (IGOM,
23 Yang and Liou, 1996) and the Amsterdam Discrete Dipole Approximation method
24 (ADDA, Yurkin et al., 2007). Surface roughness is applied only in the IGOM
25 computation ($D_{max} > 10 \mu\text{m}$), and ten prescribed roughness parameter (σ^2) values
26 are used in calculations: 0, 0.03, 0.05, 0.1, 0.15, 0.2, 0.3, 0.4, 0.5, and 0.7. The column

1 aggregate shape is chosen because the most extensive previous study on a global
2 scale (Cole et al., 2014) implies that this habit produces the most consistent
3 agreement with observations. In addition, this habit is used in the retrieval scheme
4 for the operational MODIS Collection 6 cloud products. This particle shape is an
5 aggregate of eight column elements that are solid hexagonal particles with slightly
6 different particle aspect ratios (originally defined in Yang and Liou 1996, see Yang et
7 al., 2013 for geometric parameters). The choice of roughness parameter is
8 somewhat arbitrary, but our intent is to outline the variation of $-P_{12}$ over the
9 course of roughness changes, including the roughness parameter used in MODIS
10 Collection 6 ($\sigma^2 = 0.5$). A gamma particle size distribution with an effective size
11 (diameter) of $60 \mu\text{m}$ and an effective variance of 0.1 is used in this study since we
12 expect little impact on our analysis due to this size distribution selection (Cole et al.,
13 2014).

14 The weights for the EOFs (EOF scores) are displayed in Fig. 6, and some original
15 and reconstructed $-P_{12}$ curves are plotted in Fig. 7. Figure 6 shows that the EOF 1
16 score is a monotonic function of the roughness parameter. Since the first EOF
17 explains most of the $-P_{12}$ variation (85.6%), it can be considered as an effective
18 roughness parameter for this shape. The relation between EOF 1 scores and the
19 natural logarithm of roughness parameters is nearly linear (Fig. 8), indicating that
20 the roughness parameter can be subsequently inferred after the inference of the
21 EOF 1 score. The straight line in Fig. 8 is the regression line defined in the form

$$\sigma^2 = \exp[-115.755 \times (\text{EOF 1 score}) - 2.3543]. \quad (5)$$

22 In addition, the EOF 2 score provides constraints on the retrieval especially for large
23 roughness parameters, while the EOF 1 score is less sensitive to the roughness vari-

1 ation. Therefore, the EOF 1 and EOF 2 scores are selected as retrieval parameters
2 related to particle roughness.

3 Another factor that can impact the roughness retrieval is atmospheric Rayleigh
4 scattering above the cloud. Above-cloud Rayleigh scattering has previously been
5 used to infer cloud top pressure from polarimetric measurements (e.g., Buriez et al.,
6 1997), with results comparable to those from O₂ A band retrievals and ISCCP (Parol
7 et al., 1999). With the POLDER instruments, Rayleigh scattering is primarily
8 detected as a spectral and directional difference of polarized reflectivities. Figure 9
9 shows the change of L_{np} at 0.865 μm , as a function of scattering angle, in response to
10 a 300 hPa change in cloud top pressure (i.e., from 200 to 500 hPa, the red line) and a
11 change of similar effect in roughness parameter (from $\sigma^2 = 0.15$ to 0.5, the dashed
12 green line). The effects of cloud top pressure and roughness parameter changes on
13 L_{np} have different directional patterns but comparable magnitudes. The variation of
14 the cloud top height must therefore be well constrained or retrieved simultaneously
15 when attempting to infer the roughness parameter.

16

17 **2.2.2 Construction of Forward Model**

18 Once the inverse problem is formulated, the next step is to construct a forward
19 model that is fast enough to be embedded in the inversion algorithm. From the
20 discussion in Section 2.1, the inverse problem is formalized as follows: (1) the
21 parameters to be inverted are the EOF 1 and EOF 2 scores, and cloud top pressure;
22 and (2) observations are MODIS-AIRS-collocated L_{np} from POLDER at central
23 channel wavelengths 0.865 μm , 0.67 μm , and 0.49 μm . To satisfy the requirements
24 for numerical efficiency, the present forward model is based on a look up table. The
25 adding-doubling radiative transfer program is used to compute L_{np} for every phase
26 function with seven atmospheric scattering optical thickness above the cloud: 0,

1 0.02, 0.05, 0.1, 0.15, 0.2, and 0.3. The result is parameterized by a simple linear
2 regression model defined as:

$$L_{np,i} = a_i + b_i x_1 + c_i x_2 \quad (6)$$

3 where x_1 and x_2 are EOF scores obtained in Sect. 2.2.1, and a_i , b_i , and c_i are regres-
4 sion coefficients for each viewing geometry, which is denoted by subscript i . The
5 linear relation between L_{np} and $-P_{12}$ in the single scattering approximation under-
6 scores the appropriateness of this formulation. The viewing geometry is gridded as
7 follows: solar zenith angles from 0° to 81° , viewing zenith angles from 0° to 75° , and
8 relative azimuth angles from 0° to 180° , with an interval of 3° for each. The regres-
9 sion is repeated for seven atmospheric scattering optical thicknesses above the
10 cloud and stored in a file so that one can apply appropriate interpolations. In this
11 way, once cloud top height and EOF scores are given, L_{np} can be obtained for each
12 specific viewing geometry and wavelength.

13 The fast model constructed in this way is accurate enough to solve our inverse
14 problem. A typical difference between an exact calculation and our forward model is
15 shown in Fig. 10. The overall accuracy is within 1×10^{-4} in terms of L_{np} and the
16 peak-to-peak variation is 5×10^{-4} even in the worst case ($\sigma^2 = 0.03$). The overall
17 error of 1×10^{-4} implies that the model bias is less than 10% of the observation
18 error given by ($\sqrt{\text{var}(L_{np})} = \sqrt{1.35 \times 10^{-6}} = 1.16 \times 10^{-3}$). The bias may be detected
19 in the residual of the inversion, but the influence on the roughness inference is
20 negligible.

21 In calculating cloud reflectivity, a single-layer homogeneous cloud is assumed,
22 and the cloud optical thickness is set to 5 (roughly the saturation point of polarized
23 reflectance). No aerosol is assumed to be present above and below clouds. As
24 optically thick cold ice clouds occur in the upper troposphere, the radiometric

1 contribution from lower tropospheric aerosols is neglected. For the same reason,
2 the surface is assumed to be dark. There may be an influence from aerosols above
3 the cloud layer, such as transported mineral dust and stratospheric sulfates, but we
4 disregard them to be in line with previous studies. The influence of such aerosol
5 layers on inferences of cloud properties is beyond the scope of this paper but should
6 be investigated in the future.

7 The adding-doubling radiative transfer program formulated by de Haan et al.
8 (1987) with significant improvements by Huang et al. (2015) is used in the
9 calculation. The first-order scattering is calculated analytically and combined with
10 the multiple scattering results from the adding-doubling model, following the TMS
11 method (Nakajima and Tanaka, 1991). Further, the cloud reflectivity is multiplied by
12 the transmissivity that changes due to ozone absorption; the transmissivity is
13 calculated from the monthly mean AIRS ozone concentration.

14 **2.2.3 Maximum Likelihood Estimation**

15 Once the inverse problem is formulated and the forward model is built, the last
16 step is to find the set of parameters for each pixel based on observations. The simple
17 but powerful maximum likelihood method with a normal error distribution is
18 appropriate for our problem because we have little knowledge about the
19 distribution of parameters. As each pixel typically contains five to eight valid views
20 (Section 2.1.2) at three wavelengths, the number of observations in each pixel
21 ranges from 15 to 24.

22 The standard deviation (SD) and correlation (Corr) of inferred parameters are
23 calculated in the framework of maximum likelihood estimation, and used to avoid
24 under-constrained inferences. The pixel is rejected if $SD(\text{EOF 1 Score}) > 0.02$,
25 $SD(\text{EOF 2 Score}) > 0.02$, or $\text{Corr}(\text{EOF 1 Score}, \text{EOF 2 Score}) > 0.3$. The standard
26 deviation and the correlation depend strongly on the observation geometry and

1 particle model and are almost independent of the observed polarized reflectivity.
2 Therefore, this rejection process can be interpreted as the refinement of pixels
3 based on the information content to achieve a reliable inference.

4 The error distribution is confirmed to be normal (see Section 2.1.1), so if the
5 problem is not strongly nonlinear, the parameters' error distributions are expected
6 to be normal as well (Rodgers, 2000). As expected, Fig. 11 demonstrates that the
7 application of the maximum likelihood method with synthetic L_{np} data results in a
8 symmetric distribution about the EOF 1 score corresponding to the true roughness
9 parameter $\sigma^2 = 0.15$. The distribution is not strictly normal because the number of
10 observations in each pixel varies, but the error distribution of each pixel is
11 theoretically derivable, as well as the confidence interval.

12 For the synthetic retrieval in Fig. 11, the median of the inverted EOF 1 score is –
13 0.00336 and the corresponding roughness parameter is $\sigma^2 = 0.14$. The interquartile
14 range of the EOF 1 score distribution is $[-0.01146:0.00476]$, which corresponds to
15 the roughness parameter range of $[0.05:0.36]$. The result indicates that our
16 approach has a practical skill in estimating the particle roughness parameter out of
17 observations superimposed with noise. This is a remarkable contrast with the
18 traditional “best-fit” approach (cf. Fig. 1).

19 The distribution of the χ^2 values for the synthetic retrieval is presented in Fig.
20 12. The χ^2 value is a variance-normalized residual squared sum that is defined for
21 each pixel, and follows the χ^2 distribution with degrees of freedom N_d if the
22 inversion is successful, where N_d is the observational degrees of freedom
23 (approximately, the number of observations in a pixel). As the χ^2 distribution of N_d
24 degrees of freedom has a peak about N_d , the distribution of the χ^2 value indicates
25 whether the inversion is successful. If the location of the peak of a distribution of χ^2
26 values is smaller than N_d , the observation error may be overestimated, and if the
27 location of the peak is larger than N_d , the observation error is underestimated, or

1 the forward model does not represent reality (Rodgers, 2000). The distribution in
2 Fig. 12 has a peak at about 12, and very few pixels have a χ^2 value over 40. This is a
3 reasonable distribution because the number of observations ($\approx N_d$) is about 15 to
4 24 for most pixels. Because the 95th percentile for the χ^2 distribution with 24
5 degrees of freedom is 36.42, it is no surprise that very few pixels have a χ^2 value
6 over 40.

7 Figures 11 and 12 demonstrate the validity of our inference framework under
8 an idealized situation, where the error distribution and the true roughness
9 parameter are constant. In application to actual satellite data, however, the true
10 roughness parameter varies from pixel to pixel while the error distribution stays the
11 same. Therefore, the distribution of the EOF 1 score must be more spread out as a
12 result of convolution of the error distribution and the true roughness parameter
13 distribution. In contrast, the χ^2 distribution is expected to be about the same. The
14 result of the application to the actual data is given in the next section.

15

16 **3. Results and Discussion**

17 **3.1 Roughness Parameter of Cold Ice Cloud over Oceans**

18 With the cloud selection criteria listed in Table 1, 79132 pixels were selected
19 for inversion. The information content was sufficient for full analysis of 23359
20 pixels, for which results are presented in this section.

21 The histogram of the inferred EOF 1 score is presented in Fig. 13 based on one
22 month of collocated PARASOL/MODIS data over extratropical (latitude $> 30^\circ$)
23 oceans during September 2005. The width of the histogram in Fig. 13 is broader
24 than the monodispersive roughness case (Fig. 11), indicating significant variability
25 in the microphysical properties of clouds. The median of the distribution is -0.0293 ,
26 corresponding to a surface roughness parameter of 2.82. The interquartile range of

1 the EOF 1 score is $[-0.0429;-0.0165]$, implying 50% of the data is within the
2 roughness parameter (σ^2) range of $[0.65:13.6]$. The result supports the use of the
3 roughened particle model in extratropical ice cloud retrievals as suggested by
4 previous studies. While our analysis is limited to very cold ice clouds over ocean, the
5 validity of using roughened crystals in the MODIS Collection 6 ice model is
6 supported, although further explorations into warmer and optically thinner clouds
7 are desirable. In general, cloud particles become more complex as the cloud
8 temperature increases (Heymsfield, 2002), thus we expect more roughened
9 particles in warmer clouds that are not included in our analysis.

10 As the roughness parameter of 2.82 lies outside of our prescribed roughness
11 parameter range (0 to 0.7), it is an estimate by extrapolation. Yet, this projection of
12 roughness parameter implies that the conventional degree of roughness may not be
13 sufficient to represent actual cloud particles with the aggregate column model. The
14 proportion of pixels that contains inferred roughness parameter $\sigma^2 > 0.7$ is 74%,
15 which also indicates the limit of this particle shape. As the accuracy of roughness
16 approximation for such a large roughness parameter is questionable, a particle
17 shape that can fit observations with less intense roughening may be suitable for the
18 representation of natural clouds.

19 The distributions of the χ^2 value in the tropics and extratropics are separately
20 presented in Fig. 14. As discussed in the previous section, a distribution of χ^2 values
21 indicates the validity of the inversion. While the distribution of the χ^2 values in the
22 extratropics shows a reasonable behavior (Fig. 14a), the distribution of the χ^2
23 values in the tropics has a very long tail with the mean χ^2 being 59.7, which is
24 unacceptably large (Fig. 14b). This long tail implies that our forward model does not
25 properly reproduce the observed L_{np} field in the tropics, presumably because some
26 underlying assumptions are not appropriate. Some possibilities that violate our
27 underlying assumptions include sub-pixel scale cloud heterogeneity, the presence of

1 ice particles with other habits or aspect ratios, their vertical heterogeneity, and
2 cloud 3-D effects. The extension of the parameter space to include other habits will
3 be investigated in future work.

4 **3.2 Possible Causes of Inference Failure in Tropics**

5 To gain a better insight into the cause of the long tail in the tropics, a case study
6 is conducted for two cloudy scenes: a typical extratropical scene and a tropical cloud
7 scene with systematically large χ^2 values. Figure 15 displays true color composites
8 from PARASOL with markers indicating the locations of detailed analysis. A green
9 circle is shown where the χ^2 value is less than the 95th percentile of the χ^2
10 distribution (reasonable deviation from the forward model), and a magenta cross is
11 shown where the χ^2 value is more than the 95th percentile (too far from the
12 forward model). The locations of the magenta crosses in Fig. 15a (typical
13 extratropics) are somewhat systematic; they appear at cloud boundaries or at
14 isolated locations. This may suggest that cloud heterogeneity and cloud 3-D effects
15 cause a small number of inference failures in the extratropics.

16 In contrast to the typical extratropical scene, magenta crosses are prevalent
17 throughout the tropical scene in Fig. 15b. Since the cloud reflectivity is comparable
18 to the typical extratropical scene, it is not likely that the inference failures are due to
19 contamination by surface reflection. Also failures cannot be fully explained by 3-D
20 effects of clouds as a few green circles appear randomly. Flaws in the assumptions
21 that depend little on the relative location in a cloud, such as cloud particle shape and
22 cloud heterogeneity (e.g. Oreopoulos, 2009), or the lack of information content due
23 to the limited scattering angle range are therefore suspected as causes of the
24 inference failure in the tropics. A separate validation using the Cloud-Aerosol Lidar
25 with Orthogonal Polarization (CALIOP) data indicated that our cloud top height

1 retrieval is not in agreement with CALIOP cloud top height data, possibly indicating
2 the limited information content.

3 **3.3 Comparison with Scattering Properties in the MODIS Retrieval Scheme**

4 By definition of our EOF scores, the inverted EOF scores translate into $-P_{12}$ on a
5 pixel-by-pixel basis. The reconstructed $-P_{12}$ reflects a variation due to observation
6 error and natural variability. To accurately interpret the result, we reconstructed
7 $-P_{12}$ from extratropical data with a precise EOF 2 score ($SD(EOF2) < 0.01$). The
8 area shaded with gray in Fig. 16 shows the interquartile range of the reconstructed
9 $-P_{12}$ which indicates that 50% of our extratropical observations fall within the
10 shade at a given scattering angle. The blue line is $-P_{12}$ for the particle shape used in
11 MODIS Collection 6, and the green line is that for the shape in MODIS Collection 5.
12 Both particle models assume a gamma distribution with effective particle size of 60
13 μm and effective variance of 0.1. The blue line (Collection 6) is closer to our
14 reconstruction, while the green line (Collection 5) significantly deviates from our
15 reconstruction. This result indicates that the particle habit adopted for MODIS
16 Collection 6 is more consistent with polarimetric observations than the habit
17 mixture used for MODIS Collection 5, for which only one of the habits includes a
18 limited degree of roughness.

19 The reconstructed $-P_{12}$ shows stronger side scattering between 80° and 120° than
20 the MODIS Collection 6 particle model. As the increasing roughness enhances side
21 scattering, weak side scattering of the column aggregate shape may be responsible
22 for the unphysically large roughness parameter in the extratropical inferences. By
23 using a shape that has stronger side scattering, it is likely that the degree of rough-
24 ness that is needed to explain the observations becomes smaller. An example of such
25 a habit mixture is shown by the thick magenta line in Fig. 16. A mixture of two habits
26 (70% column aggregate particles with roughness parameter of $\sigma^2 = 0.8$ and 30%

1 severely roughened hollow bullet rosette particles with $\sigma^2 = 0.5$) included in the
2 scattering property library by Yang et al. (2013), results in a phase function with
3 strong side scattering.

4 **4. Summary and Future Directions**

5 In this study, the particle roughness parameter of very cold ice clouds over
6 ocean is inferred by employing a new framework that is resilient to the
7 observational error. The distinct feature of the framework is the continuous
8 parameter space that is constructed with an empirical orthogonal function (EOF)
9 analysis. Two EOFs are found to be sufficient to explain the variation of $-P_{12}$ with a
10 changing particle roughness parameter, substantially reducing the number of
11 parameters for the forward model.

12 From unpolarized cloud reflection at a scattering angle of 170° , the
13 observational error of the PARASOL data is empirically estimated. Supported by the
14 error analysis with parametric bootstrapping, the maximum likelihood method is
15 applied to the inverse problem. The method provides error estimates and
16 correlations for inverted parameters, which are unavailable with the “best-fit”
17 approach used in the previous studies. To correctly incorporate the effect of
18 atmospheric Rayleigh scattering, the cloud-top height is inferred simultaneously.

19 The application of the present method to cold ice clouds over extratropical
20 oceans results in a roughness parameter of 2.82, implying that the use of the
21 roughened particle model is suitable for cloud property retrievals. By contrasting
22 the distribution of χ^2 values in the tropics and extratropics, we find that the
23 performance of our method needs to be enhanced in the tropics. Possible future
24 technical improvements may be an extension of parameter space to include multiple
25 particle shapes, application to optically thin clouds, and integration with
26 unpolarized radiance observations.

1 The reconstructed $-P_{12}$ curve shows better consistency with $-P_{12}$ from the
2 particle shape model used in MODIS Collection 6 than $-P_{12}$ from MODIS Collection
3 5. The addition of roughness and a hollow bullet rosette particle shape to the MODIS
4 Collection 6 model further improves the consistency.

5 Since its launch in 2004, the PARASOL satellite observed global polarimetric
6 reflectivity nearly simultaneously with MODIS for five years until leaving the A-train
7 constellation in 2009. A large amount of PARASOL data is available to apply the
8 framework described in this paper. Local variations of the roughness parameter,
9 correlation of the roughness parameter to other meteorological data, and the impact
10 of cloud heterogeneity are to be investigated in our future study.

11 **Acknowledgements**

12 The authors thank the ICARE Data and Service Center for providing
13 POLDER/PARASOL data, the NASA LAADS system for providing MODIS atmosphere
14 products, and the NASA GSFC GES DAAC for providing AIRS data. The ice particle
15 scattering calculations are conducted at the Texas A&M University Supercomputing
16 Facility. The authors are grateful to Dr. Lei Bi for help in light scattering
17 computations. This work was funded by NASA Grants NNX11AR06G and
18 NNX15A12H, and the authors are grateful for continued support from Dr. Hal
19 Maring.

20

1

2 **References**

3 Baran, A. J. and Francis, P. N.: On the radiative properties of cirrus cloud at solar and
4 thermal wavelengths: A test of model consistency using high-resolution airborne
5 radiance measurements. *Quart. J. Roy. Meteor. Soc.*, 130, 763–778, doi:
6 10.1256/qj.03.151, 2004

7 Baran, A. and C.-Labonnote, L.: On the reflection and polarisation properties of ice
8 cloud, *J. Quant. Spectrosc. Ra.*, 100, 41–54, 2006.

9 Baran, A. J. and C.-Labonnote, L.: A self-consistent scattering model for cirrus. I: The
10 solar region, *Quart. J. Roy. Meteor. Soc.*, 133, 1899–1912, 2007.

11 Baum, B. A., Yang, P., Hu, Y. X., and Feng, Q.: The impact of ice particle roughness on
12 the scattering phase matrix, *J. Quant. Spectrosc. Ra.*, 111, 2534–2549, 2010.

13 Buriez, J. C., Vanbauce, C., Parol, F., Goloub, P., Herman, M., Bonnel, B., Fouquart, Y.,
14 Couvert, P., and Seze, G.: Cloud detection and derivation of cloud properties from
15 POLDER, *Int. J. Remote Sens.*, 18, 2785-2813, doi: 10.1080/014311697217332,
16 1997.

17 Chepfer, H., Brogniez, G., and Fouquart, Y.: Cirrus clouds' microphysical properties
18 deduced from POLDER observations, *J. Quant. Spectrosc. Ra.*, 60, 375–390, 1998.

19 Cole, B. H., Yang, P., Baum, B. A., Riedi, J., and C.-Labonnote, L.: Ice particle habit and
20 surface roughness derived from PARASOL polarization measurements, *Atmos.*
21 *Chem. Phys.*, 14, 3739–3750, 2014.

22 Cole, B. H., Yang, P., Baum, B. A., Riedi, J., C.-Labonnote, L., Thieuleux, F., and Platnick,
23 S.: Comparison of PARASOL observations with polarized reflectances simulated
24 using different ice habit mixtures, *J. Appl. Meteor. Climatol.*, 52, 186–196, 2013.

1 Deschamps, P., Bréon, F., Leroy, M., Podaire, A., Bricaud, A., Buriez, J. C., and Sèze, G.:
2 The POLDER mission – instrument characteristics and scientific objectives, IEEE
3 T. Geosci. Remote, 32, 598–615, 1994.

4 de Haan, J. F., Bosma, P. B., and Hovenier, J. W.: The adding method for multiple scat-
5 tering calculations of polarized light, *Astron. Astrophys.* 183, 371–391, 1987.

6 Evans, M. J. and Rosenthal, J. S., *Probability and statistics: The science of uncertainty*,
7 2nd ed., W. H. Freeman and Company, 2010.

8 Fougnie, B., Bracco, G., Lafrance, B., Ruffel, C., Hagolle, O., and Tinell, C.: PARASOL in-
9 flight calibration and performance, *Appl. Opt.*, 46, 5435–5451, 2007.

10 Heymsfield, A. J., Bansemmer, A., Field, P. R., Durden, S. L., Stith, J. L., Dye, J. E., Hall, W.,
11 and Grainger, C. A.: Observations and parameterizations of particle size distribu-
12 tions in deep tropical cirrus and stratiform precipitating clouds: Results from in
13 situ observations in TRMM field campaigns, *J. Atmos. Sci.*, 59, 3457–3491, 2002.

14 Heymsfield, A. J., Schmitt, C., and Bansemmer, A.: Ice cloud particle size distributions
15 and pressure-dependent terminal velocities from in situ observations at temper-
16 atures from 0° to -86°C, *J. Atmos. Sci.*, 70, 4123–4154, 2013.

17 Holz, R. E., Platnick, S., Meyer, K., Vaughan, M., Wind, G., Dutcher, S., Ackerman, S.,
18 Heidinger, A., Amarasinghe, N., Wang, C., and Yang, P.: Resolving cirrus optical
19 depth biases between CALIOP and MODIS using IR retrievals. *Atmos. Chem. Phys.*,
20 submitted Sept. 2015.

21 Huang, X., Yang, P., Kattawar, G., and Liou, K. N.: Effect of mineral dust aerosol aspect
22 ratio on polarized reflectance, *J. Quant. Spectrosc. Ra.*, 151, 97–109, 2015.

23 Inoue, T.: A Cloud type classification with NOAA 7 split-window measurements, *J.*
24 *Geophys. Res.*, 92, 3991–4000, 1987.

1 King, M. D., Menzel, W. P., Kaufman, Y. J., Tanré, D., Gao, B.-C., Platnick, S., Ackerman,
2 S. A., Remer, L. A., Pincus, R., and Hubanks, P. A.: Cloud and aerosol properties,
3 precipitable water, and profiles of temperature and water vapor from MODIS,
4 IEEE T. Geosci. Remote, 41, 442–458, 2003.

5 Knap, W. H., C.-Labonnote, L., Brogniez, G., and Stammes, P.: Modeling total and po-
6 larized reflectances of ice clouds: evaluation by means of POLDER and ATSR-2
7 measurements, Appl. Opt., 44, 4060–4073, 2005.

8 C.-Labonnote, L., Brogniez, G., Buriez, J.-C., Doutriaux-Boucher, M., Gayet, J., and
9 Macke, A.: Polarized light scattering by inhomogeneous hexagonal monocrystals:
10 Validation with ADEOS-POLDER measurements, J. Geophys. Res., 106, 12139–
11 12153, 2001.

12 Liu, C., Yang, P., Minnis, P., Loeb, N., Kato, S., Heymsfield, A., and Schmitt, C.: A two-
13 habit model for the microphysical and optical properties of ice clouds, Atmos.
14 Chem. Phys., 14, 13719–13737, 2014.

15 Macke, A., and Mishchenko, M. I.: Applicability of regular particle shapes in light
16 scattering calculations for atmospheric ice particles. Appl. Opt., 35, 4291-4296,
17 doi:10.1364/AO.35.004291, 1996.

18 Macke, A., Mueller, J., and Raschke, E.: Single scattering properties of atmospheric ice
19 crystals, J. Atmos. Sci., 53, 2813–2825, 1996.

20 Mapes, B. E., and Houze, R. A.: Cloud clusters and superclusters over the oceanic
21 warm pool, Mon. Weather Rev., 121, 1398–1415, 1993

22 Masuda, K., Ishimoto, H., and Takashima, T.: Retrieval of cirrus optical thickness and
23 ice-shape information using total and polarized reflectance from satellite meas-
24 urements, J. Quant. Spectrosc. Ra., 75, 39–51, 2002.

1 Masuda, K. and Takashima, T.: Feasibility study of derivation of cirrus information
2 using polarimetric measurements from satellite, *Remote Sens. Environ.*, 39, 45–
3 59, 1992.

4 Minnis, P., Heck, P. W., and Young, D. F.: Inference of cirrus cloud properties using
5 satellite-observed visible and infrared radiances. Part II: Verification of theoret-
6 cal cirrus radiative properties, *J. Atmos. Sci.*, 50, 1305–1322, 1993.

7 Minnis, P., Sun-Mack, S., Young, D. F., Heck, P. W., Garber, D. P., Chen, Y., Spangen-
8 berg, D. A., Arduini, R. F., Trepte, Q. Z., Smith, Jr., W. L., Ayers, J. K., Gibson, S. C.,
9 Miller, W. F., Hong, G., Chakrapani, V., Takano, Y., Liou, K.-N., Xie, Y., and Yang, P.:
10 CERES Edition-2 cloud property retrievals using TRMM VIRS and Terra and Aqua
11 MODIS data - Part I: Algorithms, *IEEE T. Geosci. Remote*, 49, 4374–4400, 2011.

12 Nakajima, T. and King, M. D.: Determination of the optical thickness and effective
13 particle radius of clouds from reflected solar radiation measurements. Part I:
14 Theory, *J. Atmos. Sci.*, 47, 1878–1893, 1990.

15 Nakajima, T. and Tanaka, M.: Algorithms for radiative intensity calculations in mod-
16 erately thick atmospheres using a truncation approximation, *J. Quant. Spectrosc.*
17 *Ra.*, 40, 51-69, 1988.

18 Neshyba, S. P., Lowen, B., Benning, M., Lawson, A., and Rowe, P. M.: Roughness met-
19 rics of prismatic facets of ice, *J. Geophys. Res.*, 118, 3309–3318, 2013.

20 Oreopoulos, L., Platnick, S., Hong, G., Yang, P., and Cahalan, R. F.: The shortwave radi-
21 ative forcing bias of liquid and ice clouds from MODIS observations, *Atmos. Chem.*
22 *Phys.*, 9, 5865–5875, 2009.

23 Parol, F., Buriez, J.-C., Vanbauce, C., Couvert, P., Sèze, G., Goloub, P., and Cheinet, S.:
24 First results of the POLDER “Earth Radiation Budget and Clouds” operational al-
25 gorithm, *IEEE T. Geosci. Remote*, 37, 1597–1612, 1999.

- 1 Platnick, S., Ackerman, S., King, M. D., et al.: MODIS atmosphere L2 cloud product
2 (06_L2), NASA MODIS Adaptive Processing System, Goddard Space Flight Center,
3 doi:dx.doi.org/10.5067/MODIS/MYD06_L2.006, 2015.
- 4 Platnick, S., King, M. D., Ackerman, S. A., Menzel, W. P., Baum, B. A., Riedi, J. C., and
5 Frey, R. A.: The MODIS cloud products: Algorithms and examples from Terra,
6 IEEE T. Geosci. Remote, 41, 459–473, 2003.
- 7 Rodgers, C. D., Inverse methods for atmospheric sounding: Theory and practice,
8 World Scientific Publishing, 2000.
- 9 Rolland, P., Liou, K.-N., King, M. D., Tsay, S.-C., and McFarquhar, G. M.: Remote sens-
10 ing of optical and microphysical properties of cirrus clouds using Moderate-
11 Resolution Imaging Spectroradiometer channels: Methodology and sensitivity to
12 physical assumptions, J. Geophys. Res., 105, 11721–11738, 2000.
- 13 Sourdeval, O., C.-Labonnote, L., Baran, A. J. and Brogniez, G.: A methodology for sim-
14 ultaneous retrieval of ice and liquid water cloud properties. Part I: Information
15 content and case study. Quart. J. Roy. Meteor. Soc., 141, 870–882, doi:
16 10.1002/qj.2405, 2015.
- 17 Ulanowski, Z., Hesse, E., Kaye, P. H., and Baran, A. J.: Light scattering by complex ice-
18 analogue crystals, J. Quant. Spectrosc. Ra., 100, 382–392,
19 doi:10.1016/j.jqsrt.2005.11.052, 2006.
- 20 Ulanowski, Z., Kaye, P. H., Hirst, E., Greenaway, R. S., Cotton, R. J., Hesse, E., and Colli-
21 er, C. T.: Incidence of rough and irregular atmospheric ice particles from Small Ice
22 Detector 3 measurements, Atmos. Chem. Phys., 14, 1649–1662, doi:10.5194/acp-
23 14-1649-2014, 2014.
- 24 Um, J. and McFarquhar, G. M.: Single-scattering properties of aggregates of bullet
25 rosettes in cirrus, J. Appl. Meteorol. Climatol., 46, 757-775, 2007.

- 1 Um, J. and McFarquhar, G. M.: Single-scattering properties of aggregates of plates,
2 Quart. J. Roy. Meteor. Soc., 135, 291-304, 2009.
- 3 van Diedenhoven, B., Cairns, B., Geogdzhayev, I. V., Fridlind, A. M., Ackerman, A. S.,
4 Yang, P., and Baum, B. A.: Remote sensing of ice crystal asymmetry parameter us-
5 ing multi-directional polarization measurements - Part 1: Methodology and eval-
6 uation with simulated measurements, Atmos. Meas. Tech., 5, 2361–2374, 2012.
- 7 van Diedenhoven, B., Fridlind, A. M., Cairns, B., and Ackerman, A. S.: Variation of ice
8 crystal size, shape, and asymmetry parameter in tops of tropical deep convective
9 clouds, J. Geophys. Res., 119, 11809–11825, 2014.
- 10 Waliser, D. E., Li, J.-L. F., Woods, C. P., Austin, R. T., Bacmeister, J., Chern, J., Del Genio,
11 A., Jiang, J. H., Kuang, Z., Meng, H., Minnis, P., Platnick, S., Rossow, W. B., Stephens,
12 G. L., Sun-Mack, S., Tao, W.-K., Tompkins, A. M., Vane, D. G., Walker, C., and Wu, D.:
13 Cloud ice: A climate model challenge with signs and expectations of progress, J.
14 Geophys. Res., 114, D00A21, doi:10.1029/2008JD010015, 2009.
- 15 Xie, Y., Yang, P., Kattawar, G. W., Minnis, P., and Hu, Y. X.: Effect of the inhomogeneity
16 of ice crystals on retrieving ice cloud optical thickness and effective particle size,
17 J. Geophys. Res., 114, D11203, doi:10.1029/2008JD011216, 2009.
- 18 Yang, P., Bi, L., Baum, B. A., Liou, K.-N., Kattawar, G. W., Mishchenko, M. I., and Cole,
19 B.: Spectrally consistent scattering, absorption, and polarization properties of
20 atmospheric ice crystals at wavelengths from 0.2 to 100 μm , J. Atmos. Sci., 70,
21 330–347, 2013.
- 22 Yang, P., Hong, G., Kattawar, G. W., Minnis, P., and Hu, Y.: Uncertainties associated
23 with the surface texture of ice particles in satellite-based retrieval of cirrus
24 clouds: Part II - Effect of particle surface roughness on retrieved cloud optical

1 thickness and effective particle size, IEEE T. Geosci. Remote, 46, 1948–1957,
2 2008b.

3 Yang, P., Kattawar, G. W., Hong, G., Minnis, P., and Hu, Y.: Uncertainties associated
4 with the surface texture of ice particles in satellite-based retrieval of cirrus
5 clouds - Part I: Single-scattering properties of ice crystals with surface roughness,
6 IEEE T. Geosci. Remote, 46, 1940–1947, 2008a.

7 Yang, P., and Liou, K. N.: Geometric-optics-integral-equation method for light
8 scattering by nonspherical ice crystals, Appl. Opt., 35, 6568–6584, 1996.

9 Yang, P., Zhang, L., Hong, G., Nasiri, S. L., Baum, B. A., Huang, H.-L., King, M. D., and
10 Platnick, S.: Differences between collection 4 and 5 MODIS ice cloud opti-
11 cal/microphysical products and their impact on radiative forcing simulations,
12 IEEE T. Geosci. Remote, 45, 2886–2899, 2007.

13 Yurkin, M. A., Maltsev, V. P., and Hoekstra, A. G.: The discrete dipole approximation
14 for simulation of light scattering by particles much larger than the wavelength, J.
15 Quant. Spectrosc. Ra., 106, 546–557, 2007.

16 Zhang, Z., Yang, P., Kattawar, G., Riedi, J. C., C.-Labonnote, L., Baum, B. A., Platnick, S.,
17 and Huang, H.-L.: Influence of ice particle model on satellite ice cloud retrieval:
18 lessons learned from MODIS and POLDER cloud product comparison, Atmos.
19 Chem. Phys., 9, 7115–7129, 2009.

20

1

2 **Tables**

3

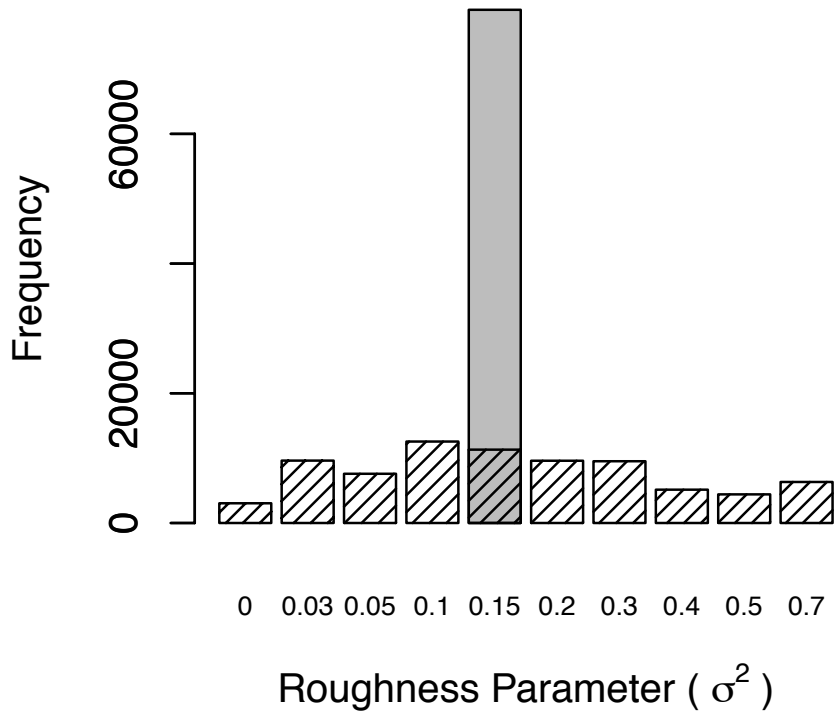
4 **Table 1.** PARASOL pixel and view selection criteria.

Parameters	Criteria	Applied to
MODIS Brightness Temperature at 11 μ m	Median is less than 208 K	Pixel
MODIS Infrared Cloud Phase	Ice	Pixel
PARASOL Ocean/Land Flag	Ocean	Pixel
Number of Valid Views	At least 5	Pixel
Scattering Angle	60° to 160°	View
Sunlint Angle	Greater than 30°	View

5

1

2 **Figures**

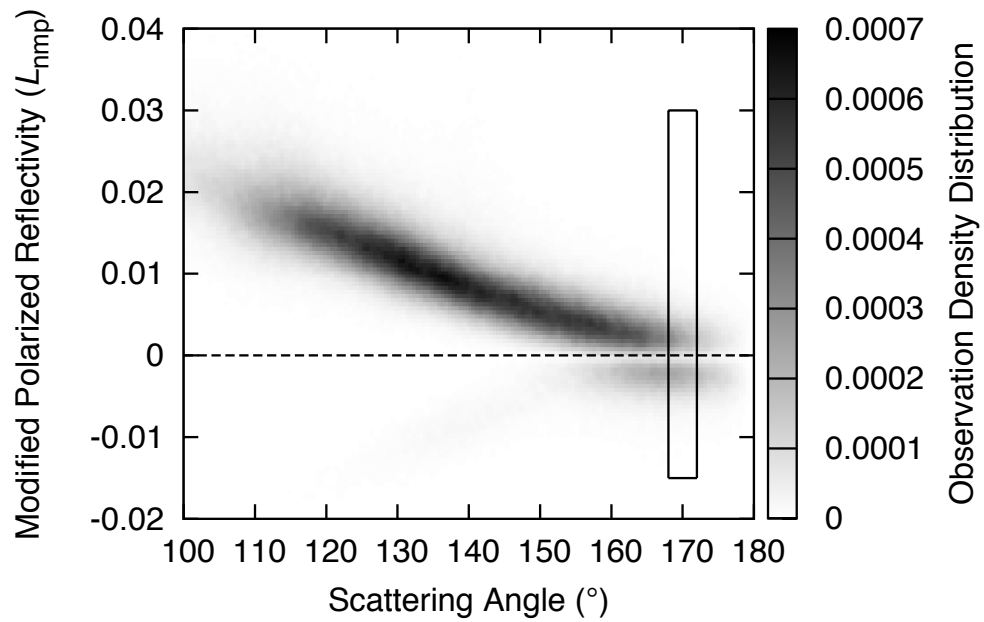


3

4 **Fig. 1.** The response of the conventional “best-fit” approach to a synthetic signal
5 with and without random measurement noise. The addition of noise to the synthetic
6 signal results in a distribution of the roughness parameter (hatched bars), from
7 which the true roughness cannot be inferred. This figure is to be compared to Fig.
8 11.

9

1

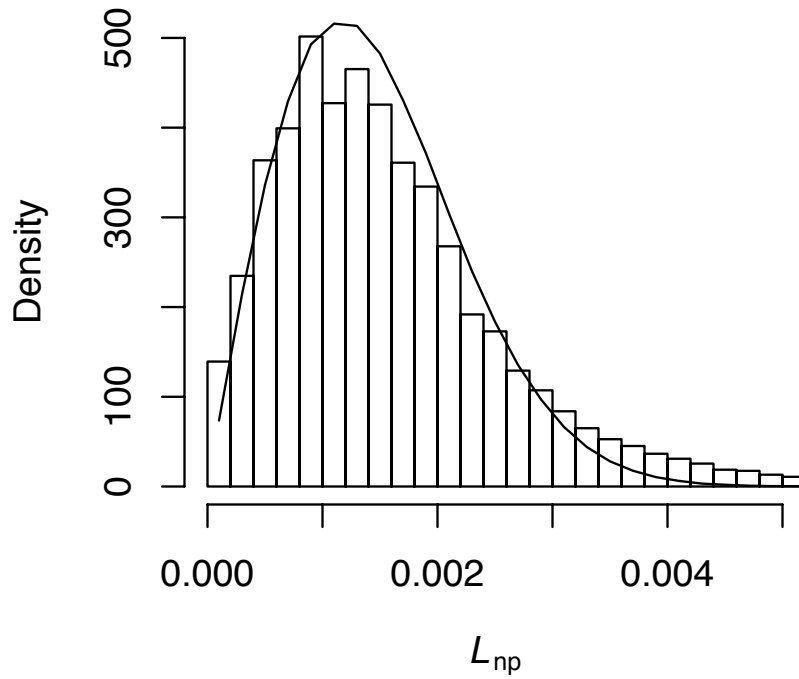


2

3 **Fig. 2.** Observation density of modified polarized reflectivity (L_{nmp}) over the West-
4 ern Pacific during September 2005. L_{nmp} crosses zero at a scattering angle of ap-
5 proximately 170°. The data in the rectangular box is used to derive the histogram in
6 Fig. 3.

7

1

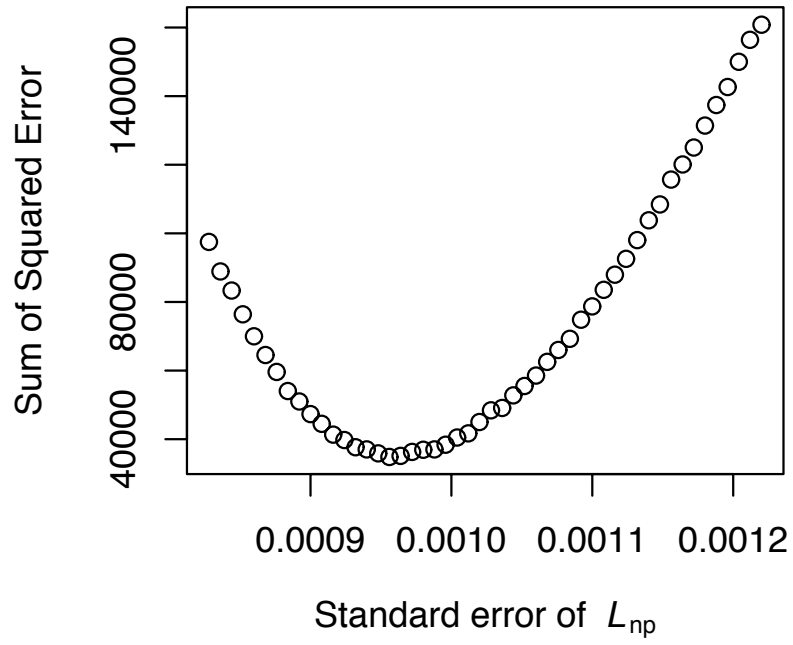


2

3 **Fig. 3.** Histogram of observed normalized polarized radiance (L_{np}) from the data in
4 the rectangular box in Fig. 2. The solid line is the simulated error using a parametric
5 bootstrapping method with $s = 0.00095$. The agreement is sufficient for estimating
6 the noise level.

7

1

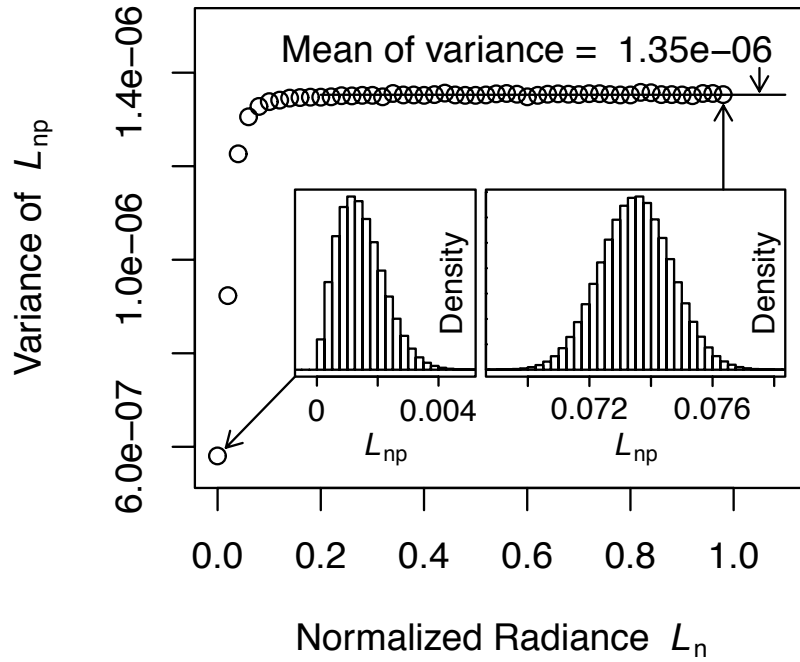


2

3 **Fig. 4.** Sum of squared error as a function of standard error (s) of the original sensor
4 noise. The minimum error is achieved when $s = 0.00095$.

5

1

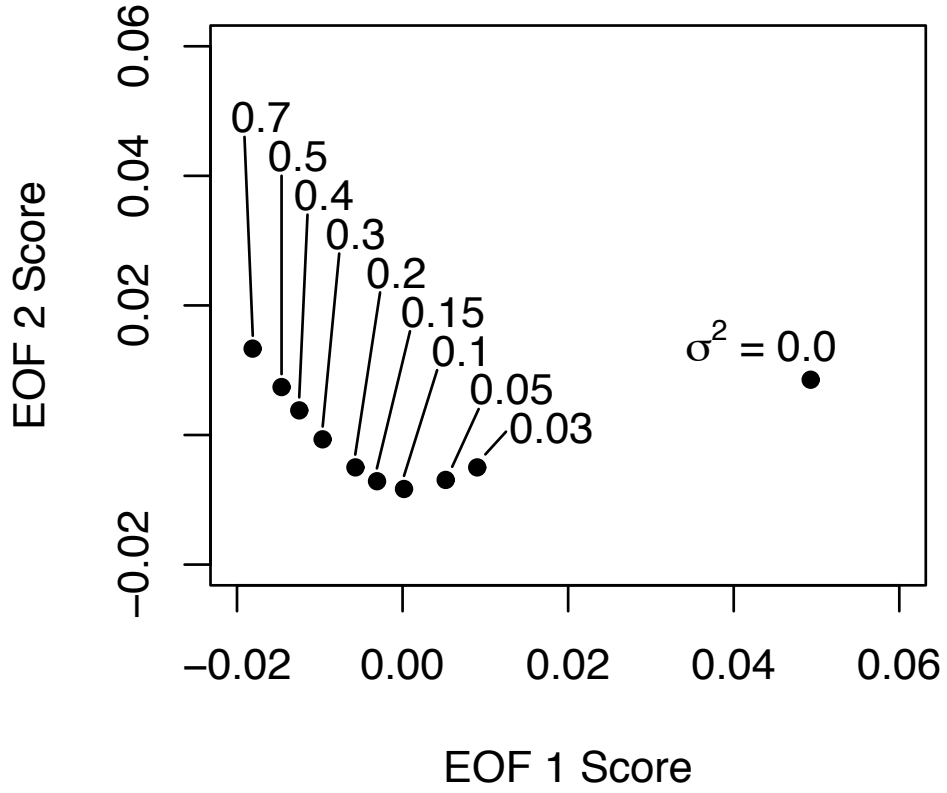


2

3 **Fig. 5.** The simulated variance of L_{np} as a function of L_n . The variance of L_{np} increas-
4 es as the normalized radiance L_n (brightness of a pixel) increases, becoming nearly
5 constant at $\text{var}(L_{np}) = 1.35 \times 10^{-6}$ once L_n reaches $L_n = 0.2$. Insets show that the
6 distribution of L_{np} tends to a normal distribution, justifying the use of a normal dis-
7 tribution as an error distribution of L_{np} for a reflective cloudy pixel.

8

1

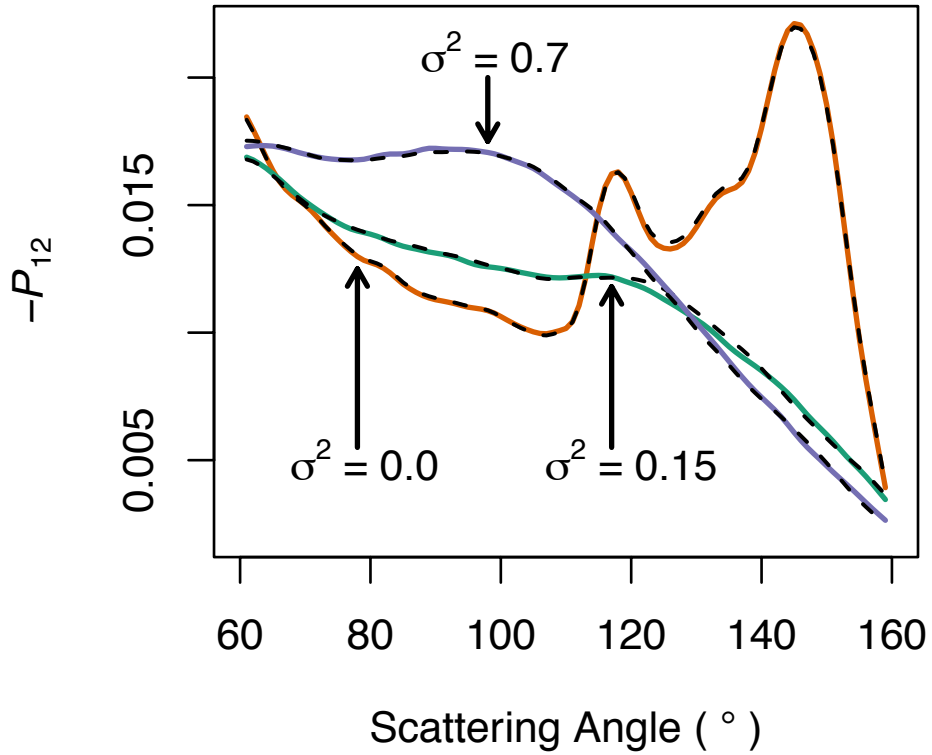


2

3 **Fig. 6.** The pairs of EOF scores needed to reconstruct the original $-P_{12}$. The EOF 1
4 score is a monotonic function of particle roughness parameter σ^2 . The EOF 2 score
5 reaches a minimum at particle roughness parameter of $\sigma^2 = 0.1$.

6

1

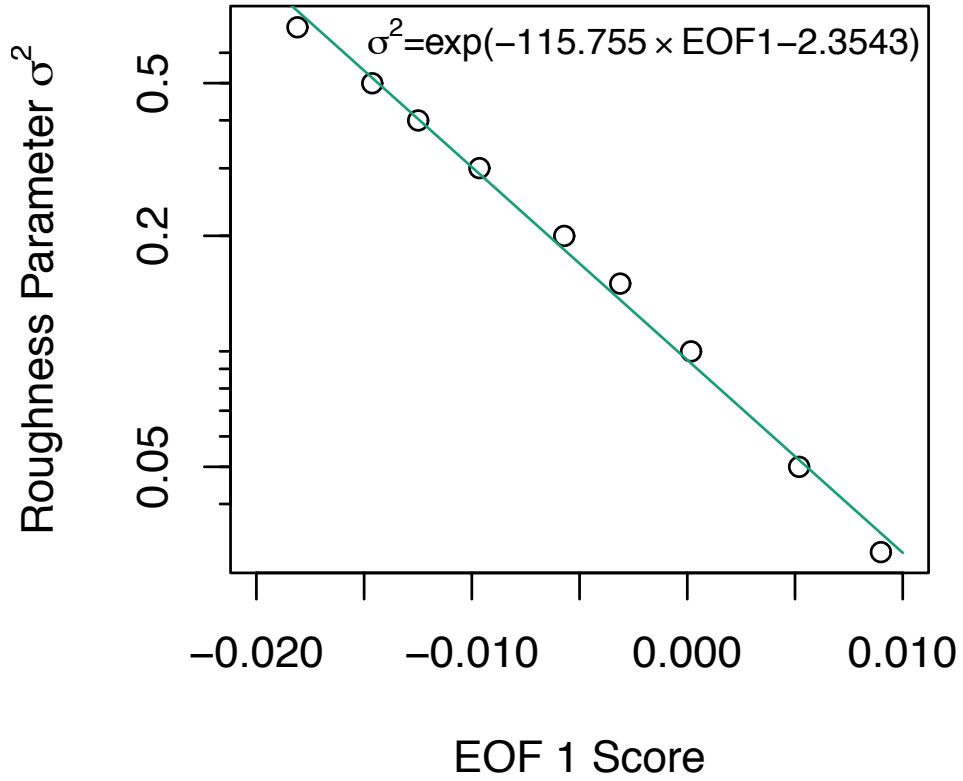


2

3 **Fig. 7.** Comparison of the reconstructed and the original $-P_{12}$ elements of the phase
4 matrix. Reconstructed $-P_{12}$ (colored solid lines) agrees with original $-P_{12}$ (black
5 dashed lines). Only the first and second EOFs are used in the reconstruction. This
6 confirms that two EOFs explain almost the entire variation of $-P_{12}$ due to the parti-
7 cle roughness change.

8

1



2

3 **Fig. 8.** The relationship between the particle roughness parameter and EOF1 score.

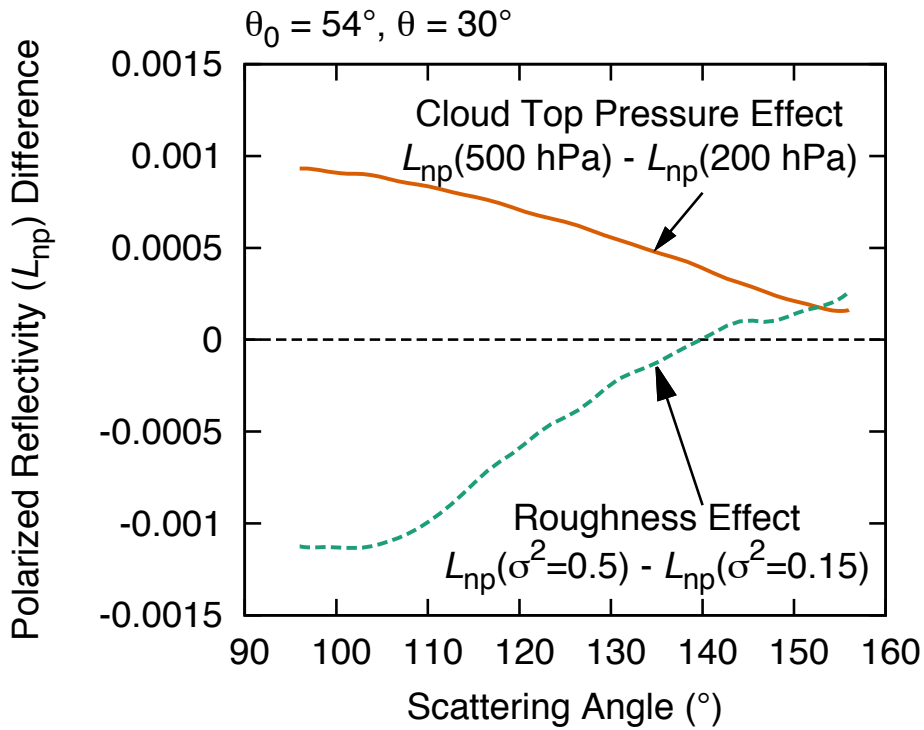
4 The natural logarithm of particle roughness parameter is nearly linear to the EOF 1

5 score. This implies that the particle roughness can be directly inferred from the EOF

6 1 score.

7

1

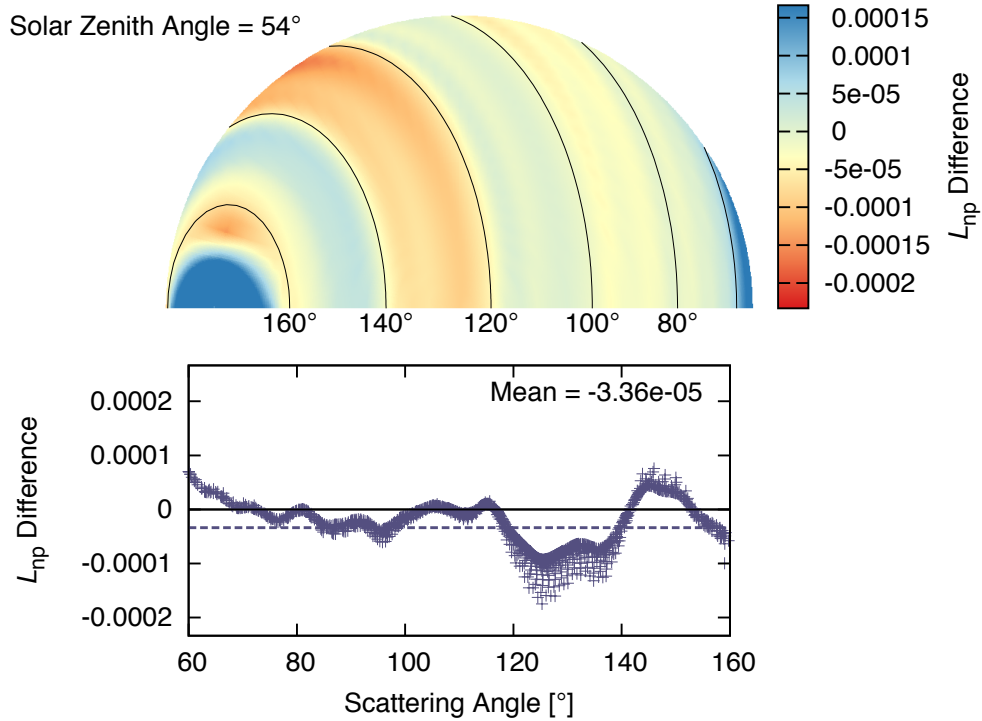


2

3 **Fig. 9.** The impact of particle roughness parameter change ($\sigma^2 = 0.15 \rightarrow 0.5$) and
4 cloud top pressure change (200 \rightarrow 500 hPa). The magnitudes of the differences are
5 comparable while the directional patterns are different. In this plot, the solar zenith
6 angle is 54° and the viewing zenith angle is 30° .

7

1

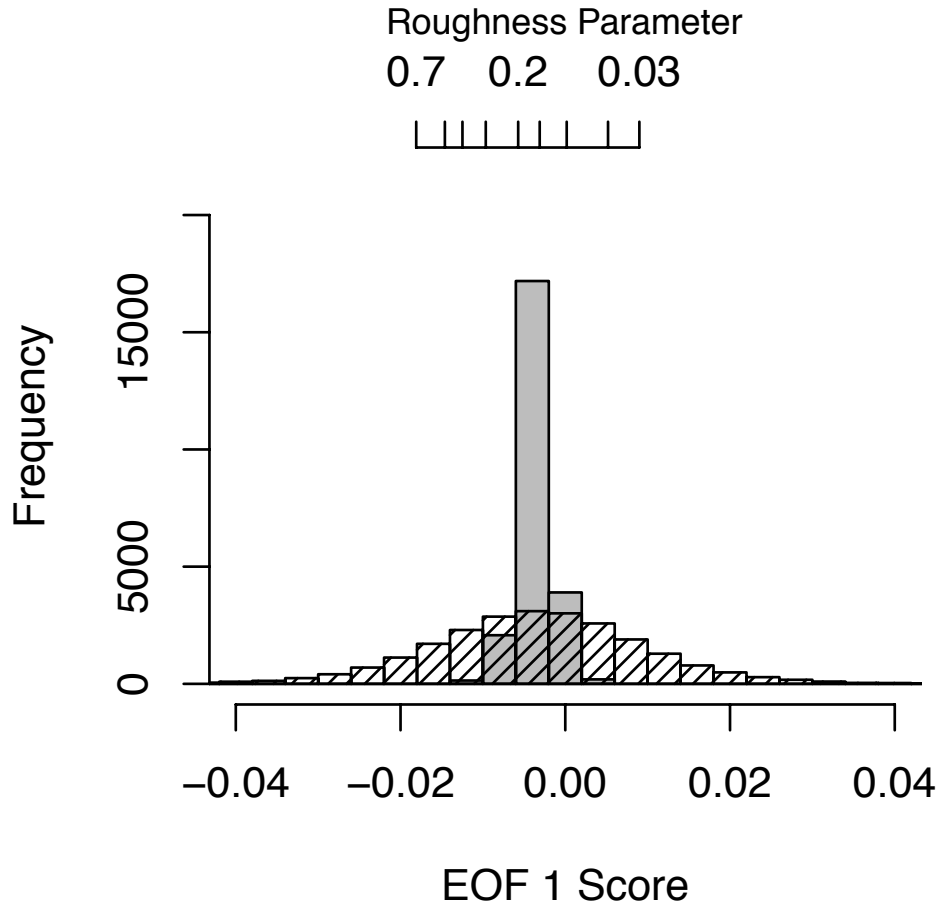


2

3 **Fig. 10.** Difference in L_{np} between exact radiative transfer calculations and our sim-
4 plified forward model. At almost all angles, the difference is less than 1×10^{-4} . The
5 polar plot shows the distribution of bias when the particle roughness parameter is
6 $\sigma^2 = 0.15$. The bias is a function of scattering angle. However, the magnitude of er-
7 ror is acceptably small compared to the random observational error.

8

1

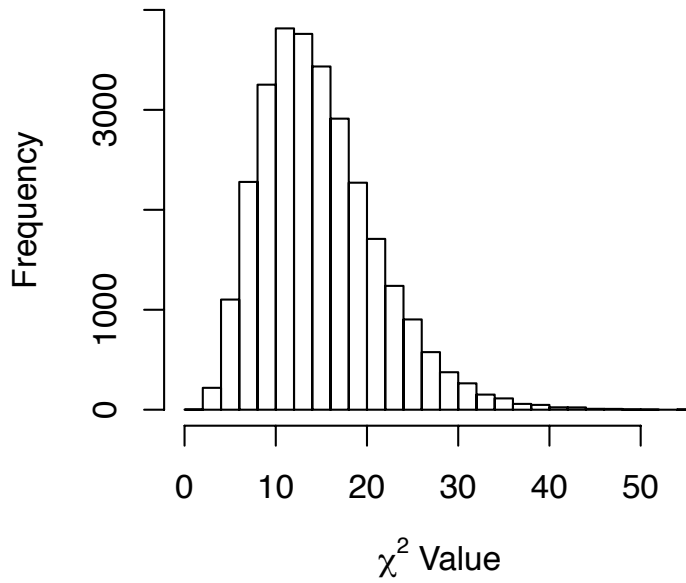


2

3 **Fig. 11.** The distribution of inferred EOF 1 scores for synthetic data with and with-
4 out noise. The distribution for the noise-added synthetic data is symmetric about
5 the EOF 1 score corresponding to the true roughness. The median of EOF 1 score is -
6 0.00336, corresponding to roughness parameter of $\sigma^2 = 0.14$.

7

1

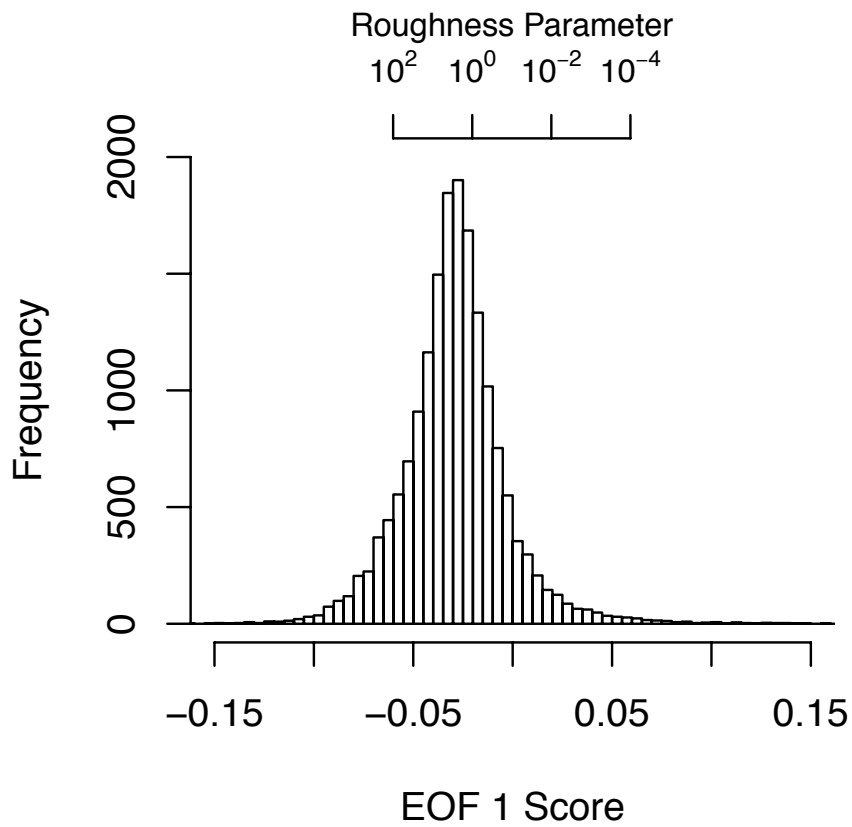


2

3 **Fig. 12.** Frequency distribution of the χ^2 values (variance-normalized residual
4 square sum). The distribution has a peak at about 12, tapering to nearly zero at ap-
5 proximately 40. This is a reasonable distribution because most pixels contain 15 to
6 24 observations.

7

1

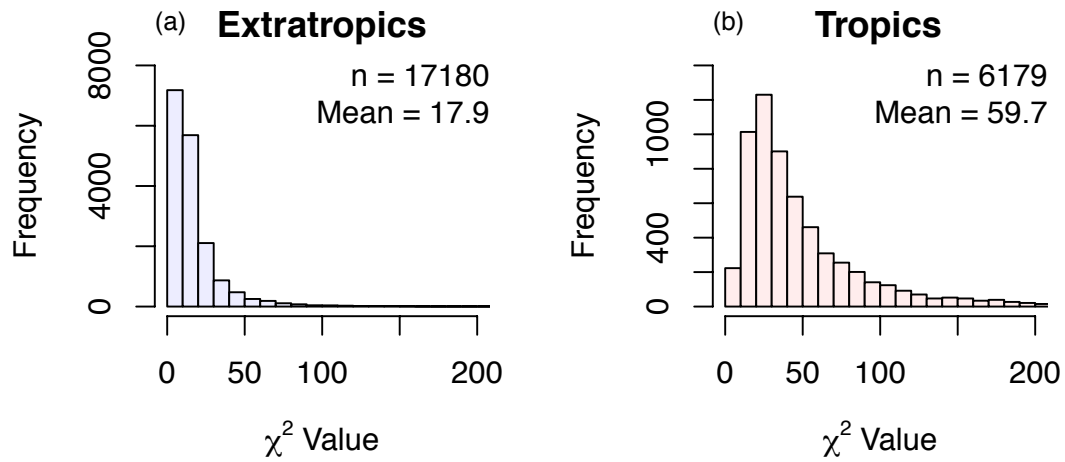


2

3 **Fig. 13.** The distribution of EOF 1 scores obtained from cold ice clouds over ocean
4 during September 2005. The median of the EOF 1 score is -0.0293 , corresponding to
5 a roughness parameter of 2.82. Consistent with previous studies, roughened parti-
6 cles better simulate the measured polarized reflectivity.

7

1

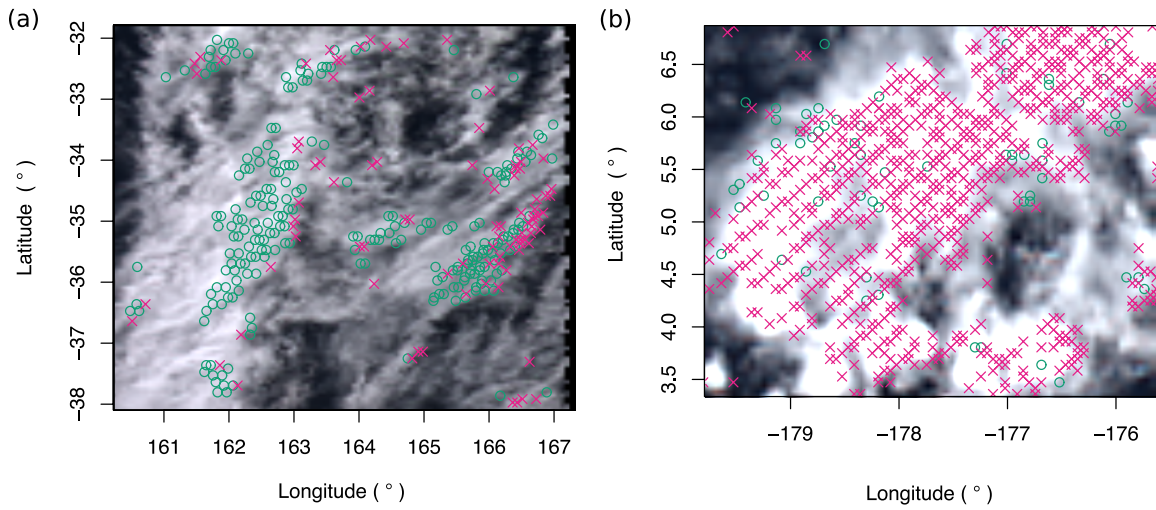


2

3 **Fig. 14.** Distributions of χ^2 values in the tropics and extratropics. The distribution of
4 the χ^2 value in the tropics (b) implies that the forward model is not correctly simu-
5 lating the reflectivity in the tropics, while the distribution of the χ^2 value in the ex-
6 tratropics (a) indicates successful inversion.

7

1

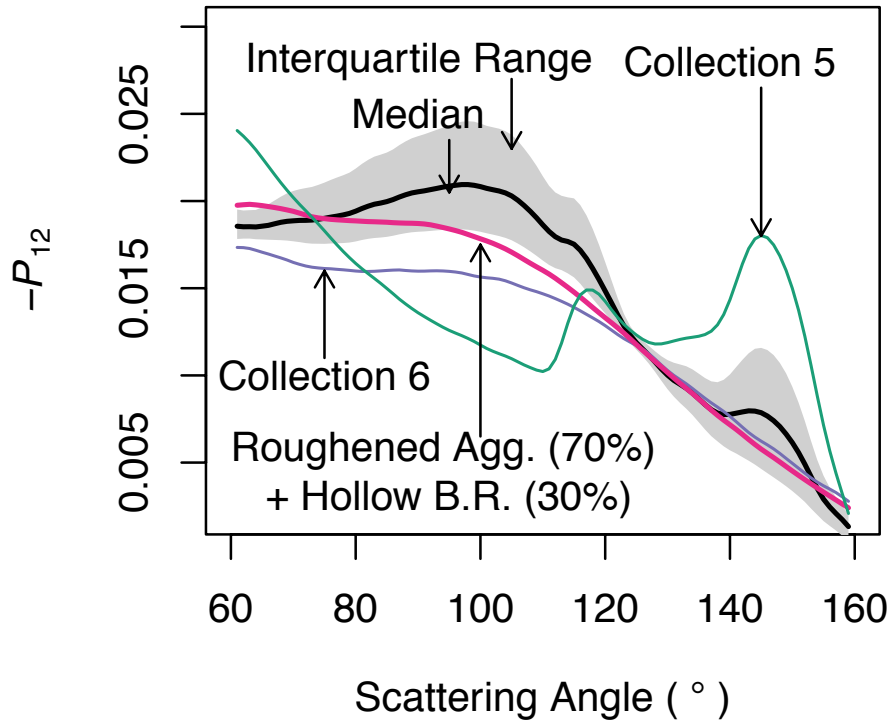


2

3 **Fig. 15.** Comparison of (a) a typical cloud scene in the extratropics and (b) a cloud
4 scene in the tropics where the χ^2 values are much larger than expected. Green cir-
5 cles are inference locations where the χ^2 value is less than 95th percentile of the χ^2
6 distribution, whereas magenta crosses are inference locations where the χ^2 value
7 exceeds the 95th percentile. These figures indicate that the causes of a large χ^2 val-
8 ue may be different in the extratropics and tropics.

9

1



2

3 **Fig. 16.** Comparison of inferred $-P_{12}$ and the counterparts used in MODIS Collec-
4 tions 5 and 6. The $-P_{12}$ of MODIS Collection 6 (blue line) is more consistent with the
5 reconstructed $-P_{12}$ (black thick line) than the $-P_{12}$ of MODIS Collection 5 (green
6 line). However, better consistency is obtained with a two-habit model (thick magen-
7 ta line), by increasing the roughness to $\sigma^2 = 0.8$ and adding 30% of hollow bullet
8 rosette particles.